Amorphous tantala and its relationship with the molten state

O. L. G. Alderman, C. J. Benmore, J. Neuefeind, E. Coillet, A. Mermet, V. Martinez, A. Tamalonis, and R. Weber

Phys. Rev. Materials **2**, 043602 — Published 23 April 2018

DOI: 10.1103/PhysRevMaterials.2.043602

Amorphous tantala and its relationship with the molten state

O.L.G. Alderman,[a,b,*] C.J. Benmore,[b] J. Neuefeind,[c] E. Coillet,[d] A. Mermet,[d] V. Martinez,[d] A. Tamalonis,[a] R. Weber[a,b]

a. Materials Development, Inc., Arlington Heights, IL 60004, USA

b. X-Ray Science Division, Advanced Photon Source, Argonne National Laboratory, Argonne, IL 60439, USA

c. Chemical and Engineering Materials Division, Oak Ridge National Laboratory, Oak Ridge, TN 37830, USA

d. Institut Lumière Matière, UMR 5306 Université Lyon 1-CNRS, Université de Lyon, F-69622 Villeurbanne, France

*Corresponding author o.alderman@gmail.com

Abstract

The structure factors of molten Ta_2O_5 and Nb_2O_5 have been measured by high-energy x-ray and pulsed neutron diffraction. These are compared to transmission-mode x-ray diffraction through a self-supported 15 µm ion-beam-sputtered amorphous tantala film. Atomistic models derived from the diffraction data by means of empirical potential structure refinement reveal that tantala and niobia liquids are very close to isomorphous, as confirmed by measurement of a molten mixture, $Ta_{0.8}Nb_{1.2}O_5$. Nonetheless, peak Nb–O bond-lengths are about 1% shorter than those for Ta–O, at temperatures, $T^* = T/T_{melt}$, scaled to the melting points. Mean coordination numbers are $n_{MO} \simeq 5.6(1)$, $n_{OM} \simeq 2.23(4)$ in the liquid state, and $n_{TaO} \simeq 6.6(2)$, $n_{OTa} \simeq 2.63(8)$ in the solid. The liquids are built from 5- and 6-fold *M*–O polyhedra which connect principally by corner-sharing, with a minority of edge-sharing. a-Ta_2O_5 on the other hand has a local structure more akin to the crystalline polymorphs, built primarily from 6- and 7-fold polyhedra, with a larger degree of edge-sharing. The structural differences between liquid and amorphous Ta_2O_5, coupled with observations of *increasing* peak bond-lengths upon cooling, are consistent with the interpretation that the amorphous film reaches a supercooled liquid-like metastable equilibrium during deposition. In other words, the amorphous film shares a common progenitor state with a hypothetical glass quenched from a fragile melt. In addition, we show that recent classical interatomic potentials do not fully reproduce the diffraction data, and infer that inclusion of attractive (non-Coulombic) Ta–Ta interactions are important, particularly for obtaining the correct degree of edge-sharing, coordination numbers and densities. Nanoscale inhomogeneity of the amorphous film is confirmed by the observation of small-angle x-ray scattering.

1. Introduction

The structure of an amorphous solid can often be influenced by its synthesis method [1-3]. Such distinct amorphous forms of a given substance are often termed polyamorphs [2], in analogy to polymorphs in the crystalline state, with perhaps the most famous example being the different forms of amorphous water ice [3]. Conversely, amorphous oxides of *similar* structure, obtained *via* different, high-energy, synthesis routes have led to the idea that a common metastable equilibrium state is reached at some point in their thermal histories [4-6]. Furthermore, this metastable state may resemble the deeply supercooled liquid, as is the case for melt-quenched glasses. Here we use high-energy x-ray and neutron diffraction to study *liquid* Ta_2O_5 and its putative isomorph – molten Nb_2O_5. Direct comparison is then made to the x-ray diffraction pattern of ion-beam-sputtered a-Ta_2O_5 obtained in transmission geometry through a 15 μm film. Such a comparison enables us to speculate on the structural relationship between the amorphous solid and hypothetical melt-quenched glass, two states often tacitly conflated in simulation studies [7-9]. Furthermore, the scattering data allow for direct testing of pair potentials used in classical molecular dynamics modelling, both in the equilibrium high temperature liquid, as well as for the non-equilibrium amorphous solid.

Amorphous tantala films have been used in the successful detection of gravitational waves, where they act as high index layers within the multilayer mirror coatings of large-scale interferometers [10-14]. For this application, among others, understanding the structural properties is key to reducing the internal friction and thermal noise and thereby increasing instrument sensitivity [14]. Amorphous transition metal oxides, including those of tantalum and niobium, are also prime candidates for use in resistive random-access memory (RRAM) [15,16] as well as electrochromic [1] and energy storage applications. As such, the structure and properties of a-Ta_2O_5 have been studied quite extensively [6,17-25]. From a glass science perspective, a-Ta_2O_5 is an intriguing material, being an 'intermediate' oxide composed of high field-strength cations, which has not been melt-quenched to form glass, but is typically formed by ion-beam sputtering. Nonetheless, glasses containing large molar amounts of Ta_2O_5 have been formed by melt-quenching [26-31], with compositions including $60Ta_2O_5{\cdot}10Ga_2O_3{\cdot}30La_2O_3$ [31], $50Ta_2O_5{\cdot}50Li_2O$ [26] and $46Ta_2O_5{\cdot}54Al_2O_3$ [28], suggesting that Ta likely partakes in network formation. Understanding the structure of high temperature melts ultimately facilitates fundamental understanding of glass-formation (and crystallization) – how and why it occurs in certain compositions and not in others.

A second aspect of this study concerns the structural similarity, or isomorphism, of molten tantala and niobia. Nb^{5+} and Ta^{5+} have identical Shannon radii (0.64 Å for *M*–O octahedra [32]), and very similar bond-valence (BV) parameters (R_{NbO} = 1.911(2) Å, R_{TaO} = 1.920(5) Å [33]), and Pauling electronegativities (χ_{Nb} = 1.6, χ_{Ta} = 1.5). The melting points of the M_2O_5 oxides differ significantly, T_{melt} = 1760 K (*M* = Nb) and 2145 K (*M* = Ta), and both are strongly polymorphic [18,34-36], in part due to the possibility of non-stoichiometry, oxygen deficiency and reduced M^{4+} states, which can lead to superlattice formation. The Ta_2O_5-Nb_2O_5 phase diagram is rather complex [37]. Whilst wide $(Ta,Nb)_2O_5$ solid-solution regions exist, these have different structures at either end of the phase diagram. Furthermore, a mixed $Nb_4Ta_2O_{15}$ phase, of unknown structure, exists over a limited temperature range above $T \approx 1680$ K, with a narrow solid-solution range. The known structures of ambient temperature M_2O_5 polymorphs typically contain *M*–O octahedra [38-42], but these are often distorted and may have additional, much longer, bonds. In

coexistence with these octahedra, 7-fold sites are also found, e.g. in high-temperature Ta_2O_5 [43], and even 4-fold tetrahedral sites, at low-abundance, in high-temperature Nb_2O_5 [44].

Given the above information, one might expect similar, though not necessarily identical structures for liquid, and even amorphous, tantala and niobia. How similar they are is an open question addressed herein. Notably the surface tensions of the two liquids are identical, and they have similar atom number densities [45].

2. Methods

2.1 Sample synthesis

A 15 µm thick layer of amorphous Ta_2O_5 was deposited at LMA (Laboratoire des Matériaux Avancés, Villeurbanne, France) with a dual ion-beam sputtering coater. The coating was deposited on a silicon substrate, an area of 1.4 mm x 1.4 mm of which was later removed by etching in order to obtain a free-standing layer.

Ceramic beads of Ta_2O_5 and Nb_2O_5, 2-4 mm in diameter, suitable for use in an aerodynamic levitation furnace, were obtained by laser melting of powders in a copper hearth open to air [46]. Starting reagents were 325 mesh Nb_2O_5 (Materion, 99.95%) and < 20 µm Ta_2O_5 (Aldrich, 99.99%). In order to obtain mixed oxide beads, the two reagents were first baked at 873 K in Pt crucibles inside an electric furnace overnight. The dried powders were then weighed into a polyethylene bottle in proportions appropriate to the desired $2Ta_2O_5{\cdot}3Nb_2O_5$ molar composition. The 1.3 g batch was then tumble mixed with a single Al_2O_3 mixing bead. The powder mixture was then formed into beads within the laser hearth as for the single oxides.

2.2 Density

The density of molten niobia has been measured by Ikemiya, et al. [45] over the $1810 \le T \le 1934$ K temperature interval, with result

$$\rho_m = 4.280 - (4.09 \times 10^{-4})(T - T_{\mathrm{melt}}) \quad (1)$$

in units of g cm^{-3} and K, and with T_{melt} = 1760 K. A contactless measurement on the more refractory liquid tantala yielded a density of 6.55 g cm^{-3} at the melting point [47]. This translates into an atom number density 93% of that for liquid niobia at T_{melt} [45]. In lieu of more accurate experimental data we derive an equation for the density of molten Ta_2O_5 based on the assumption of identical atom number density to liquid Nb_2O_5, at temperatures, $T^* = T/T_{\mathrm{melt}}$, scaled to the melting points. This procedure yields

$$\rho_m = 7.116 - (5.58 \times 10^{-4})(T - T_{\mathrm{melt}}) \quad (2)$$

where T_{melt} = 2145 K.

Densities of amorphous tantala films have been measured between 7.30 g cm^{-3} to 7.68 g cm^{-3} [19,24,25,48]. For our analyses herein we have used the larger value of 7.68 g cm^{-3} [24,25]. Note that our proposed equation (2) for the density of molten Ta_2O_5 extrapolates to a room-temperature density

of 8.15 g cm^{-3}, higher than measurements on amorphous films. This is exactly as should be expected because a hypothetical tantala glass, derived by quenching the melt, would have a smaller thermal expansion coefficient than the liquid, and therefore a lower density than the extrapolation of the liquid density curve. In addition, a-Ta_2O_5 films could be measured to have lower than their bulk densities if any porosity is present.

2.3 X-ray diffraction

High-energy x-ray diffraction experiments were performed at beamline 6-ID-D of the APS (Advanced Photon Source, Argonne, IL, USA). Pair weighting factors for the different sample compositions are given in Table 1. Cation-cation pair scattering typically dominates, followed by metal-oxygen and only a small contribution from O–O. Initial experiments used an x-ray energy of 100.315 keV (λ = 0.123595 Å), with beam cross-section 200 μm high by 500 μm wide. X-rays were detected by an a-Si Perkin-Elmer XRD1621 (2048 × 2048 pixels of 200 μm × 200 μm Tl-doped CsI scintillator) at a distance of 345.05 mm from the sample, calibrated with a cerium dioxide powder standard, giving access to a maximum $Q = (4\pi/\lambda)\sin\vartheta$ of $Q_{max} \simeq 24$ $Å^{-1}$ at scattering angle $2\vartheta_{max} = 27.3^{o}$. Only the above plane scattering was analyzed, owing to the increased absorption below the plane arising from the alignment of the x-ray beam at the top of the spheroidal sample. For Ta-bearing samples, a 1.5 mm thick sheet of brass was used in front of the detector to selectively filter out fluorescence x-rays from the Ta K-edge. Samples were held within the converging-diverging conical nozzle of an enclosed aerodynamic levitation furnace [49]. Either pure O_2 or Ar gases were used to levitate the samples, at flow rates of ≈ 0.5 L/min. The different gases allow for comparison of measurements at different oxygen partial pressures to check for any influence of reduction of $M^{5+} \rightarrow M^{4+}$ at high temperature. Heating and melting were achieved using a 500 W, 10.6 μm, CO_2 laser impinging onto the top of the sample bead, where the x-ray beam also passes, and where sample temperature was measured by optical pyrometry in the 0.9 μm near-infrared region. Apparent temperature was corrected using a Wien's displacement law approximation [50] with a spectral emissivity value of 0.87 estimated from the Fresnel losses for a material with a refractive index of 2.1 [51,52]. Correction was also made for reflection losses from a silica window and lens that were in the optical path. Measurements were made at fixed laser power, and were close to isothermal, Table 2. After initial melting, the temperature was typically lowered in 100 K steps, with measurements of 1 minute duration (3 captures using 0.2 s exposures averaging over 100 frames) at each step. Background measurements of the empty furnace were made, with either argon or oxygen gas flowing into the chamber.

The mixed oxide, $Ta_{0.8}Nb_{1.2}O_5$, sample was measured later with a slightly different set-up. X-ray energy was 100.250 keV (λ = 0.123675 Å), with beam cross-section 200 μm high by 400 μm wide. The sample-to-detector distance was 378.49 mm. The molten sample was measured in O_2 for 10 minutes in total during a single run (30 captures using 0.2 s exposures averaging over 100 frames).

Repeat measurements were made at the higher x-ray energy of 131.737 keV (λ = 0.0941149 Å), with beam cross-section 200 μm high by 500 μm wide and sample-to-detector distance of 654.04 mm. The use of higher energy x-rays reduces the absorption and fluorescence problems associated with tantalum, but comes at the expense of greatly reduced x-ray beam intensity. Oxygen was used as the

levitation gas and measurements lasted 5 minutes (15 captures using 0.2 s exposures averaging over 100 frames).

Sample masses changed very little during each run, typically remaining within the measurement uncertainty of ± 0.1 mg, or about ± 0.1%. The largest change was observed for a Ta_2O_5 sample run several times in O_2, at Δm = –0.21mg, or –0.25%.

The amorphous tantala film, with self-supported area of 1.4 mm x 1.4 mm, was suspended vertically and measured at 9 points on its surface using an incident beam cross-section of 250 µm by 250 µm. The x-ray energy was 100.315 keV (λ = 0.123595 Å), and sample-to-detector distance was 329.76 mm. Of the diffraction patterns obtained at different locations, all showed some Bragg spots arising from residual Si substrate. The measurement with the smallest Si contribution was chosen for analysis, and the Bragg spots masked out of the data. A comparison of masked and un-masked data is given in Fig. S1 [53]. The silicon contribution is very small, and any remaining diffuse scattering can be neglected in the data analysis. Later measurements for comparison were also made at 131.737 keV (λ = 0.0941149 Å), and sample-to-detector distance of 682.81 mm, as well as at 60.0673 keV (λ = 0.206409 Å), which is below the Ta K-edge (67.416 keV). Here the sample-to-detector distance was 469.46 mm. This final setup extended the measurement to lower Q, with concomitant reduction in Q_{max}.

Two dimensional diffraction data were reduced, integrated and corrected using Fit2D [54], additional angle and energy dependent corrections according to Ref. [55], and finally GudrunX [56] to obtain the x-ray structure factors. Residual background intensity varying slowly with Q was removed using the top-hat convolution method (6.0 $Å^{-1}$ top-hat width) and real-space intensity below 1.0 Å was suppressed [56]. This amounts to an aesthetic correction which is nonetheless helpful for direct comparison to modelled functions.

2.4 Neutron diffraction

The coherent neutron scattering cross-sections for Ta and Nb are similar to that for oxygen, in contrast to the case for x-rays where the heavy metal atoms dominate, see Table 1. As such, combined neutron and x-ray scattering from tantalum and niobium pentoxide are highly complementary, and allow access to information from all three pair terms, *M*–*M*, *M*–O and O–O. Moreover, the close similarity of the bound neutron coherent scattering lengths of Ta and Nb mean that measurements on both of the M_2O_5 liquids make for a direct test of their putative isomorphism.

Neutron diffraction measurements were made at the NOMAD beamline [57] of the SNS (Spallation Neutron Source, Oak Ridge, TN, USA). A re-entrant well containing an aerodynamic levitation furnace similar to that described in Ref. [58] was used. Argon was used to fill the well and as levitation gas, on account of its reduced neutron scattering compared to air or oxygen, and thereby background scattering was reduced. The neutron beam was collimated and aligned to pass above the top of an Al nozzle within which the sample was floated. Measurements of vanadium beads of varying diameter, placed in the levitator nozzle, were used for normalization to absolute units. Each liquid was measured for a total of 60 minutes. After background subtraction, absorption corrections and normalization, a further small renormalization, following the procedure in Refs [59,60] was applied. This procedure forces the low *r*

slope of $D(r)$ to be consistent with that expected based on the melt density. Finally, a Fourier filter was applied to reduce high-frequency noise and a small remaining low-frequency background. Comparisons of the data before and after this procedure are given in Fig. S2 [53].

2.5 Empirical potential structure refinement

Structural models were derived from the diffraction data using EPSR [61,62]. For the liquids, neutron and x-ray data were both used as input simultaneously, whilst for the amorphous solid, only x-ray data were available. Initial random configurations of 4900 atoms were equilibrated using Monte Carlo under Coulombic plus Lennard-Jones 12-6 reference potentials to give reasonable starting points for the refinements. The reference force-field parameterizations were based on the Lorentz-Berthelot mixing rules and the following atomic parameters: ε_O = 0.92 kJ mol^{-1}, σ_O = 3.16 Å, $q_O = -e$, ε_M = 2.23 kJ mol^{-1}, σ_M = 1.48 Å and $q_M = +2.5e$, where e is the proton charge. Temperatures and densities were fixed at 2458 K, 6.941 g cm^{-3} for Ta_2O_5, 1975 K, 4.192 g cm^{-3} for Nb_2O_5, or 298 K and 7.680 g cm^{-3} for a-Ta_2O_5. Following equilibration, empirical potential refinement was used to progressively modify the atomic configuration such that the experimental scattering data were reproduced. Once the goodness-of-fit was minimized, statistical structural data were collected over ensembles of > 2 x 10^3 configurations. It was necessary to enforce a minimum Ta–Ta separation in the models of a-Ta_2O_5, and ultimately three models were produced with different $r_{\mathrm{TaTa}}^{\mathrm{min}}$, or maximum energy amplitudes of the empirical potential, see Table 3.

2.6 Molecular dynamics

Pair potentials for Ta_2O_5 have been developed by Trinastic, et al. [8] and used by those authors [7] and others [9] to predict the structure and properties of a-Ta_2O_5. Trinastic *et al*. based their potentials on the O–O pair potential for BKS silica [63] which takes the Buckingham form. An additional Morse interaction term was included for Ta–O, whilst Ta–Ta pairs interacted solely *via* Coulombic forces. The Ta–O pair potential was fitted to lattice and elastic constants of β-Ta_2O_5 derived from density functional theoretic calculations [34].

Herein we compare existing models of a-Ta_2O_5 [8,9] to our x-ray diffraction data, and use the Trinastic *et al*. potentials, and derivatives thereof, to model molten tantala. The simulations were conducted using the DL_POLY classic code [64] in the isothermal-isobaric (NPT) ensemble at 2400 K and 1 atm pressure. An initial configuration of 1400 atoms was derived using a Monte Carlo procedure under the EPSR reference potentials described above. An equilibration period (forces capped) of 25 ps was followed by a 50 ps production run from which results were derived. A time-step of 1 fs was used throughout.

A modified set of potentials were derived, starting from those of Trinastic *et al*. These were based on the as-published Ta–O pair potential, an increased O–O Buckingham interaction amplitude A_{OO} = 2110.935 eV, and inclusion of an attractive Ta–Ta pair interaction of the form:

$$\varphi_{TaTa}(r) = A_{TaTa}\exp\left(\frac{-r}{\rho_{TaTa}}\right) - \frac{C_{TaTa}}{r^6} - \frac{D_{TaTa}}{r^8} \quad (3)$$

with A_{TaTa} = 2.4 x 10^4 eV, ρ_{TaTa} = 0.25 Å, C_{TaTa} = 1.6 x 10^3 eV Å^6 and D_{TaTa} = –1.6 x 10^3 eV Å^8. The modified potentials were derived in order to obtain the correct system density, as given by eqn. 2, and to improve

the agreement with diffraction data, primarily in terms of the nearest neighbor Ta–Ta distance distribution.

3. Results

3.1 Reciprocal-space functions

Comparison of the *Q*-weighted structure factors, or interference functions, plotted in Fig. 1, reveals a number of insights. Firstly, the great similarity between the two neutron diffraction measurements lends strong support to the idea that the tantala and niobia liquids are isomorphic. The bound neutron coherent scattering lengths (Table 1) of Ta and Nb differ by only ~2%, and as such the structure factors are expected to differ beyond this level only if the atomic arrangements themselves do so. The similarity carries over into the x-ray scattering functions, but in this case the larger number of electrons of the Ta atoms (Z_{Ta} = 73) leads to a larger weighting of the *M*–*M* pair scattering compared to Nb (Z_{Nb} = 41), see Table 1. Therefore there are clear differences in the modulation of the relative peak heights between the Ta_2O_5, Nb_2O_5 and $Ta_{0.8}Nb_{1.2}O_5$ liquids in the x-ray scattering curves.

A second insight garnered from Fig. 1 is that the effect of temperature, at least over the ~300K range explored, is small for both molten tantala and niobia. Although the structure factors at this scale are barely distinguishable between different temperature points, some subtle systematics do exist and will be explored in the discussion.

Thirdly, the a-Ta_2O_5 x-ray diffraction data reveal a much greater degree of ordering compared to the liquids, as is expected from the greatly reduced thermal disordering at room-temperature. The first peak also becomes clearly split into two peaks at 1.87 $Å^{-1}$ and 2.42 $Å^{-1}$, something not observed in related materials such as a-HfO_2 [65].

It is also evident in Fig. 1 that the x-ray data for liquid tantala are somewhat noisier than for liquid niobia. This is a consequence of the greater absorption cross-section of Ta_2O_5 *cf*. Nb_2O_5. The measurements were made using x-rays with energies greater than those of the K-edges of Nb (18.986 keV) and Ta (67.416 keV). At 100 keV, the absorption length of molten Ta_2O_5 (0.40 mm) is almost an order of magnitude smaller than for molten Nb_2O_5 (3.03 mm) and the fluorescence energy (~57 keV) and yield is correspondingly greater. This results in an attenuated signal, as well as a fluorescence background for the Ta_2O_5 measurements which increase the uncertainty in the result.

Comparison of x-ray diffraction measurements made in oxygen and argon atmospheres, Fig. S3 [53], reveals negligible changes due to the change in oxygen partial pressure, from 1 atm down to ~10^{-6} atm in UHP Ar. This implies that thermal reduction of pentavalent M^{5+} to lower valence states can be neglected in our structural analyses. Nonetheless, while materials processed in O_2 appeared white on recovery, those melted in argon were blackened, implying a small abundance of M^{4+} defects, sufficient to strongly influence the optical properties. The slightly larger changes observed for molten Ta_2O_5 compared to Nb_2O_5 are attributed to the lower signal-to-noise of the former measurements, rather than any difference in redox behavior.

X-ray diffraction measurements were conducted at 100 keV and 132 keV and direct comparisons are plotted in Fig. S4 [53]. The higher energy measurements were undertaken in order to reduce the absorption and fluorescence associated with tantalum. However, despite this advantage, the incident x-ray flux is also lowered by almost 2 orders of magnitude, which could not practically be fully compensated for by increasing the measurement times. As such, the 132 keV measurements have a lower signal-to-noise ratio, and serve mainly to verify the 100 keV measurements, without improving upon them.

The structure factor of a-Ta_2O_5 is plotted in Fig. S1 [53], where it can be seen that at $Q \lesssim 0.8$ Å^{-1} the intensity increases from a minimum value. This can be seen more clearly in the 60 keV data, Fig. S5 [53], which extend to lower Q by virtue of the lower energy and longer sample-detector distance. This small angle x-ray scattering (SAXS) implies inhomogeneity within the amorphous film, possibly nanoscale porosity built in during the deposition process. A much larger SAXS signal has recently been observed in a-HfO_2 grown by gas phase condensation [65].

3.2 Real-space functions

Total correlation functions are plotted in Fig. 2. Again, a comparative inspection reveals a remarkable amount of information, even beyond that gleaned from the reciprocal-space data plotted in Fig. 1. Perhaps the most striking feature is the split Ta–Ta nearest neighbor peak in a-Ta_2O_5, with clearly resolved peaks at 3.312(2) Å and 3.750(1) Å. The area ratio of short to long Ta–Ta distances is approximately 1:2 and they are loosely ascribed to edge- and corner-sharing TaO_n polyhedra respectively. The shorter metal-metal distance remains present as an unresolved shoulder in the x-ray data for the Ta_2O_5-Nb_2O_5 liquids.

The *M*–O nearest neighbor peaks are clearly asymmetric, with modal distances *circa* 1.9 Å and a tail, or shoulder, to higher *r*. This asymmetry of the *M*–O bond length distribution is common to many molten and amorphous oxides [65-68], with the exceptions being the highest field strength, network-forming cations such as Si^{4+} and B^{3+}. Notably the peak position is slightly larger in a-Ta_2O_5 compared to the liquids, possibly indicative of a higher average *M*–O coordination. Analysis of the full bond length distributions is made by EPSR, see below. The modal peak positions have been extracted using PFIT [69], by fitting the leading edge up to 1.95 Å, and these are recorded in Table 2 and Fig. 3. The shorter distances in the liquids compared to the solid film are clear, and indeed a larger cutoff radius of 2.0 Å was required in fitting the data for the solid. Also revealed is a difference between the niobia and tantala liquids, whereby the Nb–O peak bond length is slightly shorter compared to Ta–O, by about 0.02 Å. The reasons for this are discussed below in section 4.1.

3.3 EPSR models

The EPSR method derives ensembles of atomic configurations at fixed density that are consistent with diffraction data. The solid curves overlaid on the data in Fig. 1 and Fig. 2 demonstrate that EPSR has been successful in deriving chemically feasible atomic arrangements in all cases. Note that for the liquids the models are more highly constrained, by both neutron and x-ray data, whereas for the a-

Ta_2O_5, only x-ray data were available, and the predicted neutron data are given at the bottom of each plot.

The real-space goodness-of-fit can be calculated using [70]

$$R_\chi(r_{k,\max}) = \left(\frac{\sum_{k,\min}^{k,\max} \left[T_{\exp}(r_k) - T_{\mathrm{mod}}(r_k) \right]^2}{\sum_{k,\min}^{k,\max} T_{\exp}^2(r_k)} \right)^{1/2}, \quad (4)$$

where subscripts 'exp' and 'mod' denote experimental and modelled functions respectively. This parameter is plotted as a function of $r_{k,\max}$ in Fig. 4 ($r_{k,\min}$ = 1.2 Å) and given numerically for $r_{k,\max}$ = 8.0 Å in Table 3. The molten Nb_2O_5 XRD data is most well reproduced, followed by the ND data, molten Ta_2O_5 XRD, and finally a-Ta_2O_5 XRD. The ordering of the XRD datasets can be rationalized based on the higher quality of the Nb_2O_5 data compared to Ta_2O_5 where absorption and fluorescence have a greater effect. The a-Ta_2O_5 is least well reproduced, despite the lack of constraint by neutron diffraction data, likely because it is more ordered – it is always easier to reproduce a highly disordered (high temperature, high entropy) structure than an ordered one.

EPSR derived partial pair distribution functions, $g_{ij}(r)$ are plotted in Fig. 5, coordination number distributions in Fig. 6 and bond angle distributions in Fig. 7. It is quite clear that the independently derived structures of molten tantala and molten niobia are very similar, they are essentially the same – isomorphic – within measurement uncertainties. Amorphous tantala however has a structure quite distinct from the high temperature melts. Indeed, the melts have mean *M*–O coordination numbers (Table 3) of 5.6, compared to $n_{\mathrm{TaO}} \simeq 6.6(2)$ in the amorphous phase. Fig. 6a shows that the melts are largely composed of 5- and 6-fold Ta or Nb, with most oxygen being 2-fold, bridging oxygen, at shared corners of *M*–O polyhedra. By contrast a-Ta_2O_5 is composed largely of 6-, 7- and some 8-fold Ta, and there are more 3-fold oxygen than 2-fold, indicating a higher degree of edge-sharing of polyhedra than in the melts.

4. Discussion

4.1 Isomorphism of molten Ta_2O_5 and Nb_2O_5

Molten tantala and niobia appear to have very similar structures at the level of the atomic arrangements, and can therefore be considered as isomorphs. An additional test of this comprises the simulation of the x-ray data for the mixed molten oxide, $Ta_{0.8}Nb_{1.2}O_5$, using the appropriately weighted partial structure factors derived from EPSR of the end-member oxides. Fig. 1 and Fig. 2 demonstrate that the diffraction data are predicted reasonably well in this manner. In fact, the real-space goodness-of-fit parameters are better than those of the pure Ta_2O_5 melt, Fig. 4.

The $g_{ij}(r)$ for the two liquids, Fig. 5, are very similar. The largest difference apparent here is in the first peak of $g_{\mathrm{OO}}(r)$. Considering that this difference is not observed in the experimental neutron data, it is not considered a feature of the real liquids. Similarly, the small differences in coordination number

distributions, Fig. 6, and the 1% difference in mean coordination numbers, Table 3, are considered below the detection limit inherent in the experiments.

A true, subtle, difference in the structures does appear in the peak bond lengths, Fig. 3 and Table 2. Specifically, the peak Nb–O bond length is shorter than the Ta–O by about 0.02 Å, across the whole range of temperatures accessed. Although the Shannon radii for Nb^{5+} and Ta^{5+} are identical to the two significant figures they are given [32], a difference is apparent in the bond-valence (BV) parameters of Nb^{5+} (1.911(2) Å) and Ta^{5+} (1.920(5) Å) [33] at the level of the third significant figure. What this means is that, for identical coordination geometries, one would expect niobium-oxygen bonds to be slightly shorter (by ~0.5%) than tantalum-oxygen bonds. Indeed, since the difference in BV parameters of Δr_{BV} = 0.009(5) Å is very similar to the difference observed experimentally Δr_{xrd} = 0.018(8) Å, it can be ascribed to the intrinsic bonding difference alone, without invoking any difference in the mean coordination numbers or geometries. Again, differences in mean coordination environments at or below the 1% level cannot be ruled out.

Aleshina, et al. [71] measured x-ray diffraction patterns from *amorphous* Ta_2O_5 and Nb_2O_5 obtained by anodic oxidation. Those authors found very similar bond-lengths of r_{NbO} = 1.98(2) Å and r_{TaO} = 1.97(2) Å, and a small difference in mean coordination number of Δn_{MO} = 0.4(3), where n_{NbO} = 7.1(2) and n_{TaO} = 7.5(2). These results are slightly inconsistent, in that r and n typically scale together (logarithmically), and the slightly smaller BV parameter for Nb^{5+} [33] implies $r_{NbO} < r_{TaO}$, for $n_{NbO} \leq n_{TaO}$. The discrepancy may simply be a result of the low real-space resolution obtained by the conventional x-ray diffraction technique, using relatively low-energy x-rays from Fe, Cu and Mo K_α transitions. Nonetheless, the results suggest similar structures for the amorphous solids, as well as for the liquids measured herein.

4.2 Structure of amorphous tantala

X-ray diffraction data presented herein reveal an amorphous tantala structure distinct from that of the high temperature melt. Beyond the decreased thermal disorder at ambient temperature, the denser solid phase also possesses more highly coordinated ions, whose polyhedra link together by edge-sharing as well as corner-sharing, the latter being predominant in the melt phase.

The structure of a-Ta_2O_5 derived herein is not as well determined as those of the liquids. This is because only x-ray data were available, the unsupported area of the film (~2 mm^2) being too small compared to beams typically used for neutron diffraction. Partly as a consequence of this, it was necessary to enforce a minimum Ta–Ta separation during EPSR modelling. a-Ta_2O_5 models A and B (Table 3) were derived with $r_{\mathrm{TaTa}}^{\mathrm{min}}$ = 2.9 Å and differ only slightly on account of the larger maximum amplitude allowed for the empirical potential in a-Ta_2O_5 B. In model C however, with $r_{\mathrm{TaTa}}^{\mathrm{min}}$ = 2.5 Å, a large change is observed in the $g_{ij}(r)$, Fig. 5, whereby the peak *circa* 2.6 Å, which manifests in $g_{TaO}(r)$ in models A and B, is replaced by short Ta–Ta distances in $g_{TaTa}(r)$ in model C. Such short Ta–Ta distances are considered unlikely in the real material given that they are not found in the crystalline polymorphs of Ta_2O_5, whilst Ta–O bonds in this region are common.

The well-resolved split Ta–Ta peak observed in real-space x-ray diffraction data for a-Ta_2O_5 (Fig. 2) is a striking feature. It is not something that is observed in ambient-pressure glass-forming oxides such as

V_2O_5 [72], P_2O_5 [73], SiO_2 [74], GeO_2 [75], B_2O_3 [76], or even As_2O_3 [77]. Common to all of these glass formers is that their metal-oxygen coordination numbers are all low enough that an open network of corner-sharing polyhedra can be built up, within which oxygen bond to an average of only 2 cations (or fewer in the case of phosphorus pentoxide). Stated concisely, for glass formers:

$$n_{OM} = \frac{c_M}{c_O} n_{MO} \leq 2 \quad (5)$$

where c_M/c_O is the metal/oxygen ratio. Eqn. 5 rearranges as:

$$n_{MO} \leq 2\frac{c_O}{c_M}. \quad (6)$$

In amorphous, but non-glass-forming oxides the above inequality does not hold and the introduction of oxygen coordinated to > 2 cations leads to mixed edge- as well as corner-sharing. This leads to two distinct populations of metal-metal distances, which are often resolved as a split peak in $g_{MM}(r)$. Such splitting is observed not only for a-Ta_2O_5, but also for a-HfO_2 [65] and a-TiO_2 [66,78], as well as glassy oxides (e.g. GeO_2) compressed to sufficiently high pressures that the *M*–O coordination increases above the $2(c_O/c_M)$ threshold [79,80]. Exceptionally, Al–Al distances in a-Al_2O_3 associated with edge- and corner-sharing are too similar to be resolved, but do lead to a clearly asymmetrical peak in $g_{AlAl}(r)$ [81-83].

Note that in related materials such as amorphous hafnia [65] the ratio of short to long metal-metal distances is rather different, being approximately 2:1 in a-HfO_2, as opposed to 1:2 in a-Ta_2O_5. This is primarily a consequence of the higher oxygen:metal ratio, c_O/c_M, in tantala. A slightly lower *M*–O coordination number in a-Ta_2O_5, $n_{TaO} \approx 6.6(2)$ (Table 3) *cf*. $n_{HfO} \approx 6.8(6)$ in a-HfO_2, would also contribute to this observation.

a-Ta_2O_5 is therefore more similar to the glass-former oxides than is a-HfO_2, inasmuch as it has a higher proportion of corner-sharing *M*–O polyhedra. It might therefore be expected that tantalum could partake in oxide network formation in glasses, to a greater degree than hafnium, under the right circumstances, and in suitable compositions. This is borne out in observations of glass formation, with as much as 60 mol% Ta_2O_5 being incorporated into glassy $La_3GaTa_6O_{21}$ [31], 50 mol% in $LiTaO_3$ [26], and many other examples of tantala-rich oxide glasses [27-31,84]. Meanwhile HfO_2 shows far less solubility in oxide glasses [85-87]. Niobium oxide can be incorporated into glasses even up to 75mol% Nb_2O_5 in $LaNb_3O_9$ glass [31,88], which, like the equilibrium Ta_2O_5-Nb_2O_5 phase diagram, is suggestive of subtle differences between Ta and Nb. Similarly, ZrO_2 tends to be incorporated to slightly higher levels in glass [30,89,90], as compared to HfO_2.

Our data are compared directly in Fig. S6 to those of Shyam, et al. [20] who employed a rather different approach for obtaining the x-ray structure factor of a-Ta_2O_5. Those authors used a grazing-incidence (GI) technique which does not require any substrate removal, probing only the top 50-100 nm of the film. Overall the results are very similar. The transmission measurement has a higher signal-to-noise ratio, which might explain the more clearly resolved split in the first diffraction peaks at 1.87 $Å^{-1}$ and 2.42 $Å^{-1}$. The reduced *Q*-range of the grazing-incidence measurement means that it is not clear if small-angle

scattering is present, as for the transmission measurement, although the lowest-Q few data points do show a slight upturn. In real-space the differences in the $T(r)$ are at the noise level. A slightly longer Ta–O peak bond-length is observed in the GI data, see also Fig. 3. However, this may come down to systematic uncertainties e.g. in calibration of the scattering geometry, rather than any real difference in structure arising from slight differences in thermal history. As such, the liquid-amorphous comparison in Fig. 3 is better made between our measurements which use very similar experimental setups. Since the GI measurement is sensitive to a depth of many 10s of nanometers, it is a bulk probe, as is the transmission measurement through the 15000 nm film, and differences on the grounds of different bulk/surface sensitivities are not expected.

Shyam, et al. [20] did not quote numerical coordination numbers, but cite a similar short-range structure to the crystalline phase also measured, likely β-Ta_2O_5, with 6-fold Ta coordination. However, based on the great similarity between the GI and transmission x-ray diffraction measurements (Fig. S6), we can conclude that our models with $n_{TaO} \approx 6.6(2)$ are consistent with both datasets. Using a combination of first-principles MD and electron diffraction, Bassiri, et al. [24] obtained an average coordination number in IBS amorphous tantala of $n_{TaO} = 6.53$, in excellent agreement with the present findings.

Aleshina, et al. [71] found $n_{TaO} = 7.5(2)$, somewhat higher than the value obtained herein. The difference could arise from the synthesis method of the anodic films, which is rather different to that for IBS films, and could lead to incorporation of water and/or hydroxyls. Furthermore, the conventional x-ray diffraction technique could be subject to larger uncertainties than those quoted. Indeed, $n_{TaO} = 7.5(2)$ is closer to the 7-fold Ta sites found in high-pressure Z-Ta_2O_5 [91,92], than to any ambient pressure polymorphs. Notably Maeng, et al. [93], based on EXAFS data, suggested a similar local structure for anodic a-Ta_2O_5 as for the β-Ta_2O_5 polymorph containing 6-fold Ta. This does not completely refute the findings of Aleshina, et al. [71] however, given that EXAFS has also yielded comparatively low $n_{TaO} \simeq 5$ in IBS a-Ta_2O_5 [18], which can be at least partially attributed to the difficulties and uncertainties associated with extraction of quantitative coordination numbers from EXAFS data. Studies using ^{17}O NMR [94] suggest an O–Ta coordination number $n_{OTa} = 2.43(12)$, as derived from the relative areas of resonances assigned to 2- and 3-fold oxygen. The corresponding $n_{TaO} = 6.1(3)$ is only slightly smaller than found herein by high-energy x-ray diffraction and EPSR.

Finally, the presence of inhomogeneity in the IBS film is implied by the observed rise in SAXS, Fig. S1 and S5 [53], which specifically suggests scattering density fluctuations on the nanometer length scale. The same conclusion has recently been reached by Hart, et al. [21] using fluctuation electron microscopy and virtual dark-field imaging. Those authors found inhomogeneity on the 5 nm length scale, and furthermore that it increased with thermal annealing. Structure on this scale is difficult to capture in atomistic models, given that even a 5 nm x 5 nm x 5 nm cube contains more than 9000 atoms. To capture any fluctuations would likely require an increase in linear dimension of an order of magnitude, which is 10^3 in volume, or a total atom count on the order of 10^7. Simultaneously modelling atomic to nanoscale (or larger) structure clearly poses a general problem in the computational modelling of materials.

4.3 Temperature dependence of the liquid structure and relationship with a-Ta_2O_5

The changes in liquid x-ray diffraction patterns with temperature are very small, partly due to the relatively small temperature ranges of $\Delta T \approx 300$ K accessed. Nonetheless, Table 2 and Fig. 3 reveal subtle, systematic trends toward shorter peak *M*–O bond lengths at higher *T*. In other melts, this phenomenon has been associated with a reduction in coordination number with increasing temperature [49,95]. The gradients obtained by linear regression are $-1.8(5) \times 10^{-5}$ Å K^{-1} and $-0.6(2) \times 10^{-5}$ Å K^{-1} for Ta–O and Nb–O respectively. These correspond to negative bond-length thermal expansion coefficients of $-10(3) \times 10^{-6}$ K^{-1} and $-3.2(9) \times 10^{-6}$ K^{-1}. These are imperfect measures, owing to the asymmetry of the *M*–O bond length distributions (see also [96]), but nonetheless can be compared instructively to the magnitude of changes observed in other systems. For example, in molten $BaTi_2O_5$, $\alpha_{TiO} = -8(2) \times 10^{-6}$ K^{-1} (from the mean r_{TiO}, not the mode) [49] and in $Na_2B_4O_7$, $\alpha_{BO} = -23(3) \times 10^{-6}$ K^{-1} (mean ≈ mode) [95,97]. Therefore the values found for α_{TaO} and α_{NbO} are entirely reasonable, and imply a reduction in n_{TaO} and n_{NbO} with increasing temperature. Note that in liquid B_2O_3 a *positive* B–O bond expansion is observed, with $\alpha_{BO} = +3.7(2) \times 10^{-6}$ K^{-1}, owing to the constancy of the B–O coordination number ($n_{BO} = 3$) [76].

A coordination number which increases during cooling is exactly what would be expected from the structural differences between liquid and amorphous tantala, *if* a-Ta_2O_5 is considered an analogue for a hypothetical melt-quenched glass. If this is indeed the case, then the Ta–O bond-length and coordination number would have to increase more rapidly during cooling in the supercooled regime, as opposed to the superliquidus regime accessed experimentally herein. The reasoning behind this statement is that the extrapolation of the linear trend in Ta–O bond-length in the melt does not reach that measured for the solid, even at 0 K, let alone at a putative glass-transition in the vicinity of 900 K (based on crystallization during annealing above this temperature [6,10]). A qualitatively similar result was found in molten $BaTi_2O_5$ [49]. This type of behavior is associated with fragile melts – those that display super-Arrhenius temperature dependence of the liquid viscosity.

The idea that amorphous materials can attain a supercooled liquid-like metastable equilibrium structure is often tacitly assumed in their computational modelling. Identical MD modelling methodologies involving melt-quenching are often applied for both amorphous materials as well as glasses (materials which experimentally melt-quench without crystallization). This concept has been advanced by Kim & Stebbins et al. [4-6,94] who have shown that amorphous materials obtained by different synthesis routes often converge upon a common structural arrangement. Notably these synthesis routes involve high energy processes, in terms of the ion kinetic energy in the IBS technique, or the thermal energy supplied during annealing of sol-gel materials. We therefore expect liquid and amorphous tantala and niobia to display a phenomenology common with other single oxides. That is, coordination numbers which decrease during cooling of the liquid until frozen in at a 'glass-transition', engendering a denser amorphous phase constructed from more highly coordinated ions. This has recently been demonstrated experimentally for some binary-oxide glass-formers [49,95] and explicitly in MD models of liquid and amorphous TiO_2 [66]. We have chosen not to perform an analogous MD study herein, based on the inability of existing, and modified, classical interatomic potentials to adequately reproduce the diffraction data, as discussed below.

4.4 Need for improved interatomic potentials

The a-Ta_2O_5 model derived by Damart, et al. [9] is compared directly to real-space x-ray diffraction data in Fig. 8. The position and asymmetry of the Ta–O peak are well reproduced. The fact that the model peak is somewhat narrower can be partially attributed to the temperature difference between the 0 K model and the room temperature x-ray measurement. However, an additional factor is the smaller Ta–O (and O–Ta) coordination numbers in the MD model, Fig. 6a. The mean n_{TaO} = 5.72 and n_{OTa} = 2.29 of the MD a-Ta_2O_5 are more similar to our experimental findings for the *liquid* than for the amorphous solid, Table 3. Larger differences are evident in the Ta–Ta peaks, Fig. 8. Although both model and experiment show a split Ta–Ta peak, the MD model has a much larger proportion of the Ta–Ta distances falling under the higher separation, 'corner-sharing', peak. This is consistent with the lower coordination numbers found for the MD model, as compared to the experiment and EPSR models (Fig. 6a).

A similar situation is observed in the liquid state. The position and asymmetry of the Ta–O peak are nicely reproduced, but the Ta–Ta peak appears biased to longer 'corner-sharing' distances. The neutron diffraction data show a less-sharp O–O peak as compared to the MD model. Notably the coordination numbers do not differ greatly between the liquid and amorphous solid states in the MD model, having mean values of n_{TaO} = 5.84 and n_{OTa} = 2.34 in the melt. This is in stark contrast to our findings, whereby a-Ta_2O_5 contains more highly coordinated ions than the melts, Table 3.

At this point the densities of the various models should be discussed. The MD potentials yield densities of amorphous tantala of 7.96 g cm^{-3} [9] to 8.10 g cm^{-3} [8] that are higher than the experimental values of 7.30 to 7.68 g cm^{-3} [19,25,48]. Whilst a degree of porosity in the amorphous films might lower their measured densities below the intrinsic bulk value, such a situation cannot be expected in the liquid state. At 2400 K, the molten tantala MD model obtained herein converged to a density of 7.86 g cm^{-3}. This is only slightly lower than the solid phase MD model, and much higher than the liquid tantala density of 6.97 g cm^{-3} predicted on the basis of measurements on molten Nb_2O_5 [45], eqn. 2. Indeed, the MD liquid is denser than a-Ta_2O_5, as measured.

Therefore it can be concluded that the MD potentials lead to models of liquid and amorphous tantala which are more dense then expected experimentally, that underestimate the thermal expansion, and that underestimate the coordination numbers and possibly their changes upon melt-quenching as well.

It should not be too surprising that the Ta–O peak is well reproduced whilst the Ta–Ta peaks are not. After all, the Ta–O potential was refined in order to reproduce the structure and elastic constants of β- and δ-Ta_2O_5, as predicted from DFT, whilst the Ta–Ta interaction was not [8].

In order to improve on the set of interatomic potentials for tantala, it seems highly likely that attractive non-Coulombic interactions between Ta–Ta pairs are necessary, in order to promote a larger degree of edge-sharing of polyhedra. Such interactions have been shown to be important in a number of other molten oxides [66,67]. Results of a preliminary refinement, including non-Coulombic Ta–Ta interactions are plotted in Fig. 8. The final density of the system was 6.98 g cm^{-3}, in excellent agreement with the predicted 6.97 g cm^{-3} [45], by construction. Whilst there is also improved agreement with the x-ray and neutron diffraction data, further room for improvement remains. It is possible that alternative forms of

the Ta–Ta potential are necessary, or else polarizable or many-body potentials may be required. Indeed, differences in the polarizability of niobium and tantalum [98,99] may be the key to explaining many of the observed differences between niobite and tantalate materials.

5. Conclusions

Neutron and x-ray scattering data have been used to test existing molecular dynamics models based on classical interatomic potentials, and to derive models by empirical potential structure refinement of liquid and amorphous tantala, as well as molten niobia, leading to the following conclusions:

i) Molten Ta_2O_5 and Nb_2O_5 are isomorphic, with any differences at or below the 1% level. Their short-range structure comprises a mixture of 5- and 6-fold metal-oxygen polyhedra which are linked primarily by corner-sharing, with a minority of edge-sharing.

ii) The main difference observed between the two melts is a Nb–O bond length 1% shorter than for Ta–O, at temperatures $T^* = T/T_{melt}$ scaled to the melting points.

iii) Amorphous tantala is denser than the liquid, and has higher coordination numbers, being built primarily from 6- and 7-fold Ta–O polyhedra which link by edge-sharing as well as corner-sharing.

iv) Ta–O and Nb–O peak bond lengths contract slightly with increasing temperature, implying a coordination decrease.

v) The structural differences between the solid amorphous and liquid states is consistent with the phenomenology observed for some other molten oxides, both glass-forming and non-glass-forming, whereby coordination numbers increase during melt-quenching to form an amorphous glassy phase. This in turn is consistent with the idea that a common progenitor metastable state is obtained during certain high-energy synthesis routes for amorphous solids, and that this may be identified with the supercooled liquid state from which traditional glasses are formed.

vi) Existing classical interatomic potentials for tantalum oxide fail to completely reproduce the scattering data and expected densities. It is suggested that attractive (non-Coulombic) Ta–Ta interactions are important, particularly for obtaining the correct degree of edge-sharing.

vii) Ion beam sputtered amorphous Ta_2O_5 causes small-angle x-ray scattering, consistent with other measurements which imply inhomogeneity on the nanometer scale. This poses another, separate, challenge for molecular dynamics modelling, since very large numbers of atoms, ~10^7, are required to capture such density fluctuations.

Future work should include: Development of improved interatomic potentials for tantalum and niobium pentoxides which reproduce experimental data, including the observed differences between analogous tantalate and niobate systems; modelling of the structural changes accompanying melt-quenching; detailed measurements and understanding of the nanometer scale inhomogeneity in a-Ta_2O_5; neutron scattering from a-Ta_2O_5 to further constrain models and to test the predicted structure factor derived herein.

Acknowledgements

Thanks to Prof. Gianpietro Cagnoli, director of the Institut Lumière Matière, France, for provision of the original amorphous tantala film. Leighanne Gallington and Sam Sendelbach are thanked for assistance with beamline measurements at the SNS and APS respectively. Thanks also to Stuart Reid of the University of the West of Scotland for bringing a-Ta_2O_5 to my attention at a 2015 meeting of the Society of Glass Technology, UK. Work was supported by U.S. Department of Energy (DOE) under grant number SBIR DE-SC0015241 (OLGA, AJT, JKRW). This research used resources of the Advanced Photon Source, a U.S. DOE Office of Science User Facility operated for the DOE Office of Science by Argonne National Laboratory under Contract No. DE-AC02-06CH11357, and of the Spallation Neutron Source, a DOE Office of Science User Facility operated by the Oak Ridge National Laboratory.

References

[1] A. Llordes, Y. Wang, A. Fernandez-Martinez, P. Xiao, T. Lee, A. Poulain, O. Zandi, C. A. Saez Cabezas, G. Henkelman, and D. J. Milliron, Nat. Mater. **15**, 1267 (2016).
[2] J. H. Cartwright, A. G. Checa, J. D. Gale, D. Gebauer, and C. I. Sainz-Díaz, Angew. Chem. Int. Ed. **51**, 11960 (2012).
[3] T. Bartels-Rausch, V. Bergeron, J. H. E. Cartwright, R. Escribano, J. L. Finney, H. Grothe, P. J. Gutiérrez, J. Haapala, W. F. Kuhs, J. B. C. Pettersson, S. D. Price, C. I. Sainz-Díaz, D. J. Stokes, G. Strazzulla, E. S. Thomson, H. Trinks, and N. Uras-Aytemiz, Rev. Mod. Phys. **84**, 885 (2012).
[4] N. Kim, R. Bassiri, M. M. Fejer, and J. F. Stebbins, J. Non-Cryst. Solids **429**, 5 (2015).
[5] N. Kim, R. Bassiri, M. M. Fejer, and J. F. Stebbins, J. Non-Cryst. Solids **405**, 1 (2014).
[6] N. Kim and J. F. Stebbins, J. Non-Cryst. Solids **378**, 158 (2013).
[7] J. P. Trinastic, R. Hamdan, C. Billman, and H.-P. Cheng, Phys. Rev. B **93**, 014105 (2016).
[8] J. Trinastic, R. Hamdan, Y. Wu, L. Zhang, and H.-P. Cheng, J. Chem. Phys. **139**, 154506 (2013).
[9] T. Damart, E. Coillet, A. Tanguy, and D. Rodney, J. Appl. Phys. **119**, 175106 (2016).
[10] I. W. Martin, R. Bassiri, R. Nawrodt, M. M. Fejer, A. Gretarsson, E. Gustafson, G. Harry, J. Hough, I. MacLaren, S. Penn, S. Reid, R. Route, S. Rowan, C. Schwarz, P. Seidel, J. Scott, and A. L. Woodcraft, Classical Quant. Grav. **27**, 225020 (2010).
[11] D. Crooks, P. Sneddon, G. Cagnoli, J. Hough, S. Rowan, M. Fejer, E. Gustafson, R. Route, N. Nakagawa, and D. Coyne, Classical Quant. Grav. **19**, 883 (2002).
[12] S. D. Penn, P. H. Sneddon, H. Armandula, J. C. Betzwieser, G. Cagnoli, J. Camp, D. Crooks, M. M. Fejer, A. M. Gretarsson, and G. M. Harry, Classical Quant. Grav. **20**, 2917 (2003).
[13] M. H. Gregory *et al.*, Classical Quant. Grav. **24**, 405 (2007).
[14] M. Granata, E. Saracco, N. Morgado, A. Cajgfinger, G. Cagnoli, J. Degallaix, V. Dolique, D. Forest, J. Franc, and C. Michel, Phys. Rev. D **93**, 012007 (2016).
[15] L. Zhu, J. Zhou, Z. Guo, and Z. Sun, J. Phys. Chem. C **120**, 2456 (2016).
[16] J. H. Ju, S. K. Jang, H. Son, J.-H. Park, and S. Lee, Nanoscale **9**, 8373 (2017).
[17] R. Bassiri, M. R. Abernathy, F. Liou, A. Mehta, E. K. Gustafson, M. J. Hart, H. N. Isa, N. Kim, A. C. Lin, I. MacLaren, I. W. Martin, R. K. Route, S. Rowan, B. Shyam, J. F. Stebbins, and M. M. Fejer, J. Non-Cryst. Solids **438**, 59 (2016).
[18] R. Bassiri, F. Liou, M. R. Abernathy, A. C. Lin, N. Kim, A. Mehta, B. Shyam, R. L. Byer, E. K. Gustafson, M. Hart, I. MacLaren, I. W. Martin, R. K. Route, S. Rowan, J. F. Stebbins, and M. M. Fejer, APL Materials **3**, 036103 (2015).
[19] N. Banno, T. Sakamoto, N. Iguchi, M. Matsumoto, H. Imai, T. Ichihashi, S. Fujieda, K. Tanaka, S. Watanabe, S. Yamaguchi, T. Hasegawa, and M. Aono, Appl. Phys. Lett. **97**, 113507 (2010).
[20] B. Shyam, K. H. Stone, R. Bassiri, M. M. Fejer, M. F. Toney, and A. Mehta, Sci. Rep. **6**, 32170 (2016).

[21] M. J. Hart, R. Bassiri, K. B. Borisenko, M. Véron, E. F. Rauch, I. W. Martin, S. Rowan, M. M. Fejer, and I. MacLaren, J. Non-Cryst. Solids **438**, 10 (2016).
[22] R. Bassiri, M. Hart, R. L. Byer, K. B. Borisenko, K. Evans, M. M. Fejer, A. C. Lin, I. MacLaren, A. S. Markosyan, and I. W. Martin, Journal of Physics: Conference Series **522**, 012043 (2014).
[23] R. Bassiri, K. Evans, K. Borisenko, M. Fejer, J. Hough, I. MacLaren, I. Martin, R. Route, and S. Rowan, Acta Mater. **61**, 1070 (2013).
[24] R. Bassiri, K. Borisenko, D. Cockayne, J. Hough, I. MacLaren, and S. Rowan, Appl. Phys. Lett. **98**, 031904 (2011).
[25] R. Bassiri, University of Glasgow, 2011.
[26] A. Glass, M. Lines, K. Nassau, and J. Shiever, Appl. Phys. Lett. **31**, 249 (1977).
[27] K. M. Wetherall, P. Doughty, G. Mountjoy, M. Bettinelli, A. Speghini, M. F. Casula, F. Cesare-Marincola, E. Locci, and R. J. Newport, J. Phys.: Condens. Matter **21**, 375106 (2009).
[28] G. A. Rosales-Sosa, A. Masuno, Y. Higo, H. Inoue, Y. Yanaba, T. Mizoguchi, T. Umada, K. Okamura, K. Kato, and Y. Watanabe, Sci. Rep. **5**, 15233 (2015).
[29] X. Ma, Z. Peng, and J. Li, J. Am. Ceram. Soc. **98**, 770 (2015).
[30] T. Suzuki and A.-M. Anthony, Mater. Res. Bull. **9**, 745 (1974).
[31] K. Yoshimoto, A. Masuno, M. Ueda, H. Inoue, H. Yamamoto, and T. Kawashima, J. Am. Ceram. Soc., In Press (2018).
[32] R. D. Shannon, Acta Crystallogr. A **32**, 751 (1976).
[33] I. D. Brown and D. Altermatt, Acta Crystallogr. **B41**, 244 (1985).
[34] Y.-N. Wu, L. Li, and H.-P. Cheng, Phys. Rev. B **83**, 144105 (2011).
[35] L. A. Reznichenko, V. V. Akhnazarova, L. A. Shilkina, O. N. Razumovskaya, and S. I. Dudkina, Crystallogr Rep+ **54**, 483 (2009).
[36] Y. Yang and Y. Kawazoe, Physical Review Materials **2**, 034602 (2018).
[37] G. Mohanty, L. Fiegel, and J. Healy, The Journal of Physical Chemistry **68**, 208 (1964).
[38] W. Mertin, S. Andersson, and R. Gruehn, J. Solid State Chem. **1**, 419 (1970).
[39] F. Laves, W. Petter, and H. Wulf, Naturwissenschaften **51**, 633 (1964).
[40] L. Aleshina and S. Loginova, Crystallogr Rep+ **47**, 415 (2002).
[41] S. Andersson, Z. Anorg. Allg. Chem. **351**, 106 (1967).
[42] T. Ercit, MinPe **43**, 217 (1991).
[43] N. Stephenson and R. Roth, J. Solid State Chem. **3**, 145 (1971).
[44] K. Kato, Acta Crystallogr. B **32**, 764 (1976).
[45] N. Ikemiya, J. Umemoto, S. Hara, and K. Ogino, ISIJ Int. **33**, 156 (1993).
[46] J. K. R. Weber, J. J. Felten, and P. C. Nordine, Rev. Sci. Instrum. **67**, 522 (1996).
[47] M. Maurakh, B. Mitin, and M. Roitberg, INDUSTRIAL LABORATORY **33**, 984 (1967).
[48] T. Li, F. A. Aguilar Sandoval, M. Geitner, L. Bellon, G. Cagnoli, J. Degallaix, V. Dolique, R. Flaminio, D. Forest, M. Granata, C. Michel, N. Morgado, and L. Pinard, Phys. Rev. D **89**, 092004 (2014).
[49] O. L. G. Alderman, C. J. Benmore, A. Tamalonis, S. Sendelbach, S. M. Heald, and R. Weber, J. Phys. Chem. C **120**, 26974 (2016).
[50] J. K. R. Weber, S. Krishnan, C. D. Anderson, and P. C. Nordine, J. Am. Ceram. Soc. **78**, 583 (1995).
[51] L. Gao, F. Lemarchand, and M. Lequime, Opt. Express **20**, 15734 (2012).
[52] T. J. Bright, J. I. Watjen, Z. M. Zhang, C. Muratore, A. A. Voevodin, D. I. Koukis, D. B. Tanner, and D. J. Arenas, J. Appl. Phys. **114**, 083515 (2013).
[53] See Supplemental Material at [URL] for comparisons of diffraction data showing effects of substrate masking, Fourier filtering, atmospheric gas composition, incident x-ray energy, small-angle x-ray scattering, and comparison to published grazing incidence x-ray diffraction.
[54] A. P. Hammersley, S. O. Svensson, M. Hanfland, A. N. Fitch, and D. Hausermann, High Pressure Res. **14**, 235 (1996).

[55] L. B. Skinner, C. J. Benmore, and J. B. Parise, Nucl. Instrum. Meth. A **662**, 61 (2012).
[56] A. K. Soper and E. R. Barney, J. Appl. Cryst. **44**, 714 (2011).
[57] J. Neuefeind, M. Feygenson, J. Carruth, R. Hoffmann, and K. K. Chipley, Nucl. Instrum. Meth. B **287**, 68 (2012).
[58] L. B. Skinner, C. J. Benmore, J. K. R. Weber, S. Tumber, L. Lazareva, J. Neuefeind, L. Santodonato, J. Du, and J. B. Parise, J. Phys. Chem. B **116**, 13439 (2012).
[59] O. L. G. Alderman, A. C. Hannon, D. Holland, and N. Umesaki, J. Non-Cryst. Solids **386**, 56 (2014).
[60] A. C. Hannon, in *Modern glass characterisation*, edited by M. Affatigato (Wiley, New York, 2015), pp. 1.
[61] A. K. Soper, Chem. Phys. **202**, 295 (1996).
[62] A. K. Soper, Phys. Rev. B **72**, 104204 (2005).
[63] B. W. H. Van Beest, G. J. Kramer, and R. A. Van Santen, Phys. Rev. Lett. **64**, 1955 (1990).
[64] W. Smith and T. R. Forester, J. Mol. Graphics **14**, 136 (1996).
[65] L. Gallington, Y. Ghadar, L. Skinner, J. Weber, S. Ushakov, A. Navrotsky, A. Vazquez-Mayagoitia, J. Neuefeind, M. Stan, J. Low, and C. Benmore, Materials **10**, 1290 (2017).
[66] O. L. G. Alderman, L. B. Skinner, C. J. Benmore, A. Tamalonis, and J. K. R. Weber, Phys. Rev. B **90**, 094204 (2014).
[67] L. B. Skinner, C. J. Benmore, J. K. R. Weber, J. Du, J. Neuefeind, S. K. Tumber, and J. B. Parise, Phys. Rev. Lett. **112**, 157801 (2014).
[68] L. B. Skinner, C. J. Benmore, J. K. R. Weber, M. A. Williamson, A. Tamalonis, A. Hebden, T. Wiencek, O. L. G. Alderman, M. Guthrie, L. Leibowitz, and J. B. Parise, Science **346**, 984 (2014).
[69] PFIT, http://www.alexhannon.co.uk/ (Accessed Jan 18 2011).
[70] A. C. Wright, in *Experimental Techniques of Glass Science*, edited by C. J. Simmons, and O. H. El-Bayoumi (The American Ceramic Society, Westerville, Ohio, 1993), pp. 205.
[71] L. A. Aleshina, V. P. Malinenko, A. D. Phouphanov, and N. M. Jakovleva, J. Non-Cryst. Solids **87**, 350 (1986).
[72] U. Hoppe, R. Kranold, and E. Gattef, Solid State Commun **108**, 71 (1998).
[73] U. Hoppe, R. Kranold, A. Barz, D. Stachel, and J. Neuefeind, Solid State Commun **115**, 559 (2000).
[74] Q. Mei, C. J. Benmore, S. Sen, R. Sharma, and J. L. Yarger, Phys. Rev. B **78**, 144204 (2008).
[75] M. Micoulaut, L. Cormier, and G. S. Henderson, J. Phys.: Condens. Matter **18**, R753 (2006).
[76] O. L. G. Alderman, G. Ferlat, A. Baroni, M. Salanne, M. Micoulaut, C. J. Benmore, A. Lin, A. Tamalonis, and J. K. R. Weber, J. Phys.: Condens. Matter **27**, 455104 (2015).
[77] Q. Mei, C. J. Benmore, E. Soignard, S. Amin, and J. L. Yarger, J. Phys.: Condens. Matter **19** (2007).
[78] V. Petkov, G. Holzhüter, U. Tröge, T. Gerber, and B. Himmel, J. Non-Cryst. Solids **231**, 17 (1998).
[79] T. T. Duong, T. Iitaka, P. K. Hung, and N. Van Hong, J. Non-Cryst. Solids **459**, 103 (2017).
[80] Y. Kono, C. Kenney-Benson, D. Ikuta, Y. Shibazaki, Y. Wang, and G. Shen, Proc. Natl. Acad. Sci. USA **113**, 3436 (2016).
[81] P. Lamparter and R. Kniep, Physica B **234**, 405 (1997).
[82] G. Gutierrez and B. Johansson, Phys. Rev. B **65**, 104202 (2002).
[83] S. Davis and G. Gutiérrez, J. Phys.: Condens. Matter **23**, 495401 (2011).
[84] T. Kokubo, M. Nishimura, and M. Tashiro, J. Non-Cryst. Solids **15**, 329 (1974).
[85] M. Imaoka, T. Yamazaki, and I. Yasui, Report of the Institution of Industrial Science, Tokyo University, Tokyo, Japan **31**, 59 (1984).
[86] T. Yamazaki, M. Imaoka, and I. Yasui, Report of the Institution of Industrial Science, Tokyo University, Tokyo, Japan **31**, 103 (1984).
[87] M. Imaoka and T. Yamazaki, Report of the Institution of Industrial Science, Tokyo University, Tokyo, Japan **24**, 27 (1975).
[88] A. Masuno, S. Kohara, A. C. Hannon, E. Bychkov, and H. Inoue, Chem. Mater. **25**, 3056 (2013).

[89] M. Imaoka and T. Yamazaki, Rep. Inst. Ind. Sci. Univ. Tokyo **6**, 127 (1957).
[90] M. Imaoka and T. Yamazaki, J. Ceram. Assoc. Japan **71**, 215 (1963).
[91] V. Filonenko and I. Zibrov, Inorg. Mater. **37**, 953 (2001).
[92] I. Zibrov, V. Filonenko, M. Sundberg, and P.-E. Werner, Acta Crystallogr. Sect. B: Struct. Sci. **56**, 659 (2000).
[93] S. Maeng, L. Axe, T. Tyson, and A. Jiang, J. Electrochem. Soc. **152**, B60 (2005).
[94] N. Kim and J. F. Stebbins, Chem. Mater. **23**, 3460 (2011).
[95] O. L. G. Alderman, M. Liska, J. Machacek, C. J. Benmore, A. Lin, A. Tamalonis, and J. K. R. Weber, J. Phys. Chem. C **120**, 553 (2016).
[96] S. V. Sukhomlinov and M. H. Müser, J. Chem. Phys. **146**, 024506 (2017).
[97] O. L. G. Alderman, C. J. Benmore, A. Lin, A. Tamalonis, and J. K. R. Weber, J. Am. Ceram. Soc., Accepted (2018).
[98] L. Ma, J. Indergaard, B. Zhang, I. Larkin, R. Moro, and W. A. de Heer, Phys Rev A **91**, 010501 (2015).
[99] T. Gould and T. Bučko, J Chem Theory Comput **12**, 3603 (2016).
[100] V. F. Sears, Neutron News **3**, 26 (1992).

Table 1: Pair weighting factors for M_2O_5 materials based on the bound neutron coherent scattering lengths $\overline{b}_O$ = 5.803(4) fm, $\overline{b}_{Ta}$ = 6.91(7) fm, and $\overline{b}_{Nb}$ = 7.054(3) fm [100]. X-ray weightings are calculated at Q = 0, where $f_i(Q = 0) \approx Z_i$ and Z_O = 8, Z_{Ta} = 73, and Z_{Nb} = 41.

Material	Radiation	Pair weighting		
		M–*M*	*M*–O + O–*M*	O–O
Ta_2O_5	X-ray	0.616	0.338	0.046
$Ta_{0.8}Nb_{1.2}O_5$	X-ray	0.531	0.395	0.073
Nb_2O_5	X-ray	0.452	0.441	0.107
Ta_2O_5	Neutron	0.104	0.437	0.459
Nb_2O_5	Neutron	0.107	0.440	0.453

Table 2: Summary of 100 keV x-ray and spallation neutron diffraction measurements on the a-Ta_2O_5 IBS film and molten Ta_2O_5-Nb_2O_5 liquids. The densities shown are derived from measurements on molten niobia by Ikemiya, et al. [45], and on the amorphous phase by Bassiri [25].

Material	Radiation	Gas	T / K	T_{melt} / K	T/T_{melt} / K/K	Density / g cm^{-3}	Density / atom Å^{-3}	r_1 / Å
Ta_2O_5	X-ray	O_2	2287(10)	2145	1.066	7.0363	0.067124	1.910(8)
Ta_2O_5	X-ray	O_2	2339(18)	2145	1.09	7.0073	0.066847	1.913(11)
Ta_2O_5	X-ray	O_2	2400(32)	2145	1.119	6.9732	0.066522	1.910(8)
Ta_2O_5	X-ray	O_2	2458(17)	2145	1.146	6.9409	0.066214	1.907(8)
Ta_2O_5	X-ray	O_2	2504(26)	2145	1.167	6.9152	0.065969	1.908(8)
Ta_2O_5	X-ray	O_2	2538(32)	2145	1.183	6.8963	0.065788	1.907(8)
Ta_2O_5	X-ray	O_2	2595(26)	2145	1.21	6.8645	0.065484	1.905(7)
$Ta_{0.8}Nb_{1.2}O_5$	X-ray	O_2	2145(10)	1941	1.105	5.3186	0.066680	1.893(3)
Nb_2O_5	X-ray	O_2	1820(11)	1760	1.034	4.2556	0.06749	1.892(2)
Nb_2O_5	X-ray	O_2	1870(11)	1760	1.063	4.2352	0.067166	1.891(1)
Nb_2O_5	X-ray	O_2	1975(21)	1760	1.122	4.1922	0.066485	1.891(2)
Nb_2O_5	X-ray	O_2	2081(13)	1760	1.182	4.1489	0.065797	1.890(2)
Ta_2O_5	X-ray	Ar	2234(16)	2145	1.041	7.0659	0.067406	-
Ta_2O_5	X-ray	Ar	2378(23)	2145	1.109	6.9855	0.066639	-
Ta_2O_5	X-ray	Ar	2478(19)	2145	1.155	6.9297	0.066107	1.924(18)
Nb_2O_5	X-ray	Ar	2071(30)	1760	1.177	4.153	0.065862	1.888(1)
a-Ta_2O_5	X-ray	Air	298(2)	2145	0.139	7.680	0.073264	1.957(6)
Ta_2O_5	Neutron	Ar	2423(25)	2145	1.130	6.9604	0.066400	1.919(4)
Nb_2O_5	Neutron	Ar	1923(25)	1760	1.093	4.2135	0.066822	1.912(5)

Table 3: Details of EPSR and MD models. Maximum amplitude of the empirical potential, U_E, minimum cation–cation separation, $r_{\mathrm{MM}}^{\mathrm{min}}$, metal–oxygen and oxygen–metal coordination numbers with standard deviations *of their distributions* in parentheses, goodness-of-fit parameters, $R\chi$. Values are given for the MD model for a-Ta_2O_5 of Ref. [9], whilst the 2400 K liquid was modelled using the refined potentials derived herein.

	EPSR					MD	
Model	a-Ta_2O_5 A	a-Ta_2O_5 B	a-Ta_2O_5 C	Ta_2O_5 2458K	Nb_2O_5 1975K	a-Ta_2O_5 [9]	Ta_2O_5 2400K
U_E (kJ/mol)	547	912	547	534	534	-	-
$r_{\mathrm{MM}}^{\mathrm{min}}$ (Å)	2.9	2.9	2.5	0.9	0.9	-	-
$n_{MO}(r_{\mathrm{cut}} = 2.75$ Å)	6.58(88)	6.74(97)	6.29(79)	5.52(63)	5.57(63)	5.72	5.84
$n_{OM}(r_{\mathrm{cut}} = 2.75$ Å)	2.63(59)	2.70(62)	2.51(56)	2.21(49)	2.23(47)	2.29	2.34
$R\chi(1.2 \le r_{\mathrm{cut}} \le 8.0$ Å) XRD (%)	3.86	3.36	2.57	3.26	1.57	22.53	10.97
$R\chi(1.2 \le r_{\mathrm{cut}} \le 8.0$ Å) ND (%)	-	-	-	2.50	2.63	-	7.47

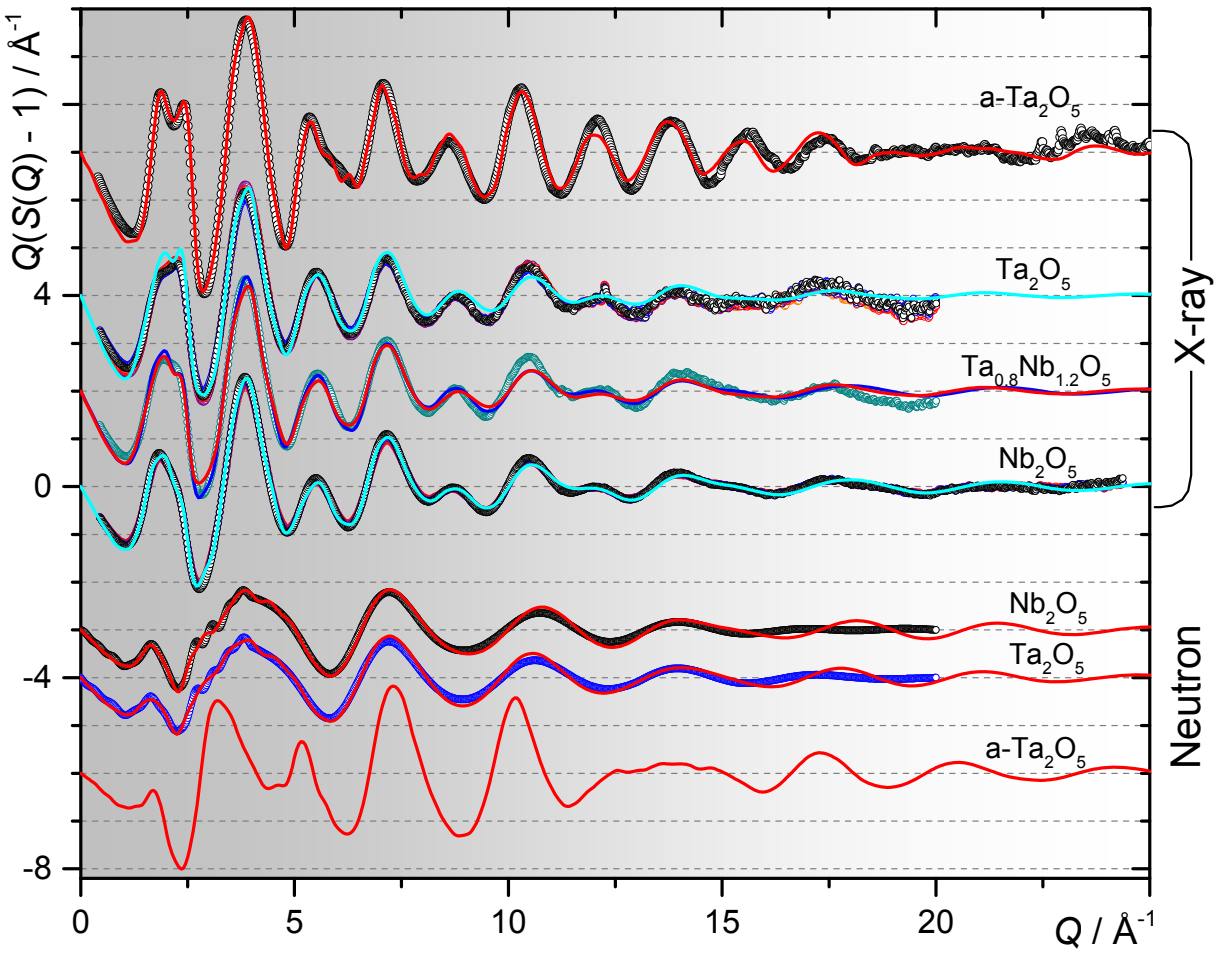

Figure 1: Interference functions, $Q(S(Q) - 1)$, for the a-Ta_2O_5 IBS film and molten Ta_2O_5-Nb_2O_5 liquids. Measurements (open points) in O_2 gas using 100 keV x-rays and in Ar gas using spallation neutrons are shown. The solid curves (red or cyan) overlaid are derived by EPSR. In the case of a-Ta_2O_5, only the predicted neutron function is shown. Seven liquid Ta_2O_5 and four liquid Nb_2O_5 datasets obtained at different temperatures are shown overlaid in different colours. For the $Ta_{0.8}Nb_{1.2}O_5$ molten solution, two solid curves are overlaid, obtained by re-weighting and summing the partial structure factors derived by EPSR for the Ta_2O_5 (red) and Nb_2O_5 (blue) endmembers, assuming isomorphism. Vertical offsets have been applied for clarity.

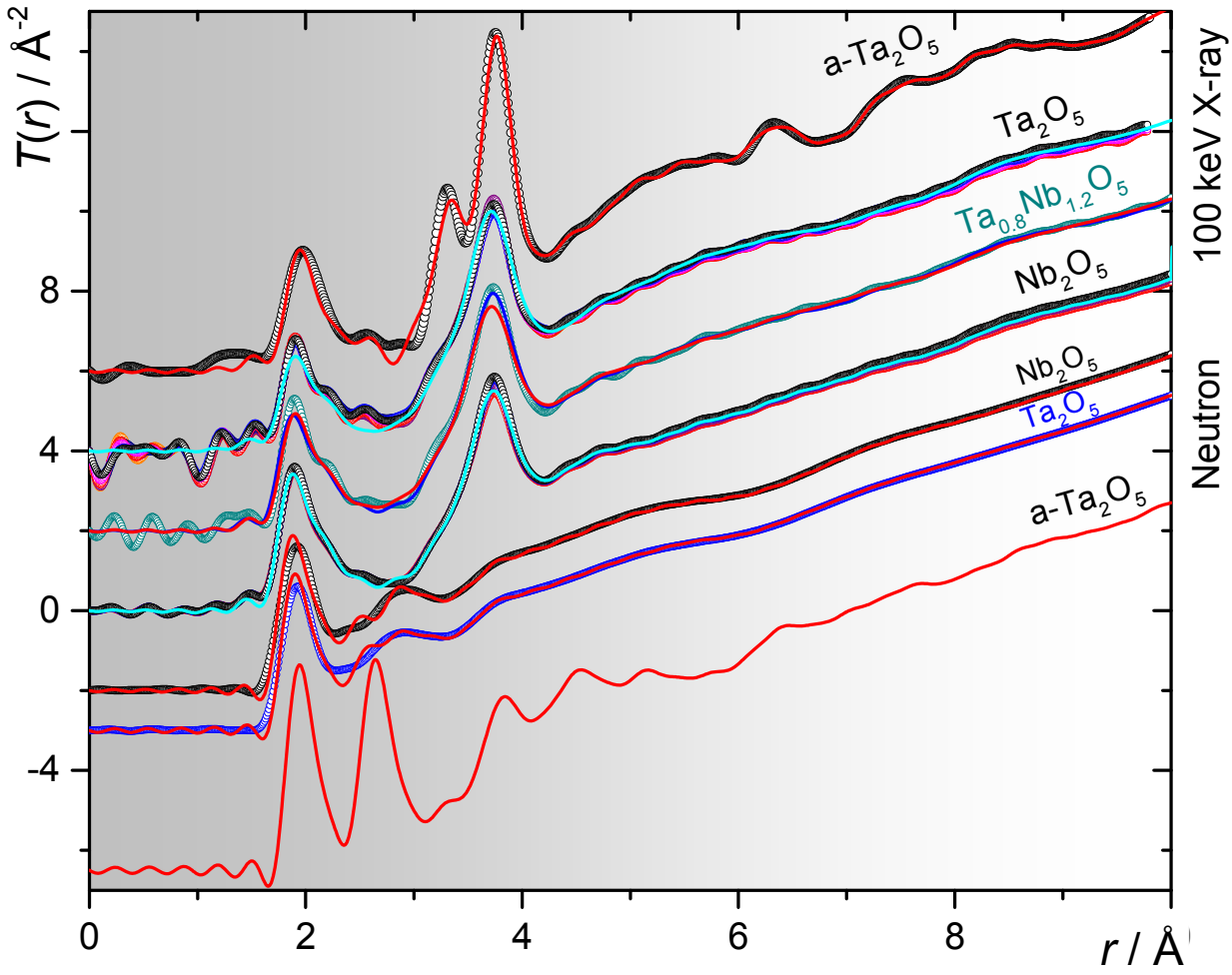

Figure 2: The total correlation functions obtained by sine Fourier transform of the data in Fig. 1. In all cases a Q_{max} = 20.0 Å^{-1} was used, without any additional window or modification function. Vertical offsets have been applied for clarity.

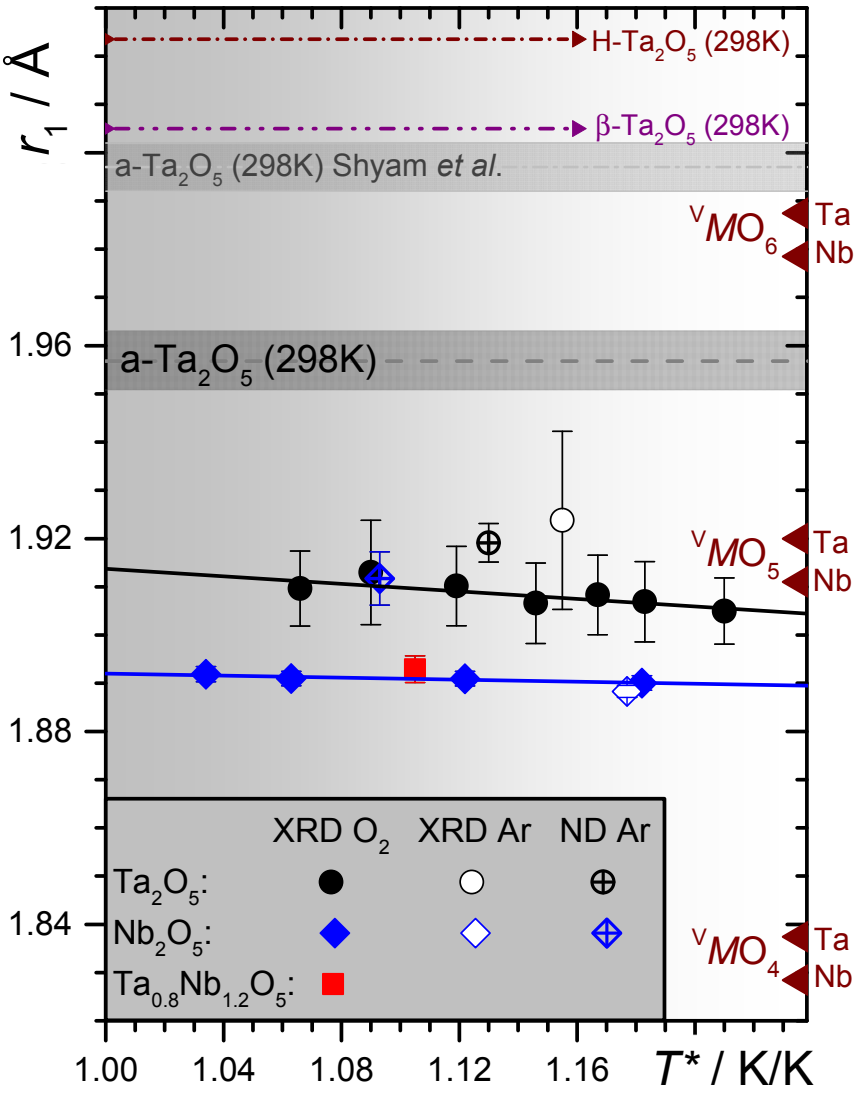

Figure 3: Peak (modal) bond lengths for a-Ta_2O_5 IBS film and molten Ta_2O_5 and Nb_2O_5 liquids, as a function of $T^* = T/T_{melt}$. Solid lines are linear regressions of the XRD data collected in O_2 gas. Crystallographic mean bond lengths for H-Ta_2O_5 [43] and β-Ta_2O_5 [40] are shown for comparison. Also shown to the right-hand side are bond-valence derived bond-lengths for 4-, 5- and 6-fold pentavalent cations, relevant to ambient temperature and calculated assuming equivalency of all bonds within the polyhedron. Note that this equivalency of bonds does not exist in the liquids or the amorphous film, where the mean and modal bond lengths differ significantly. Nonetheless, the bond-valence derived values serve as a useful reference point.

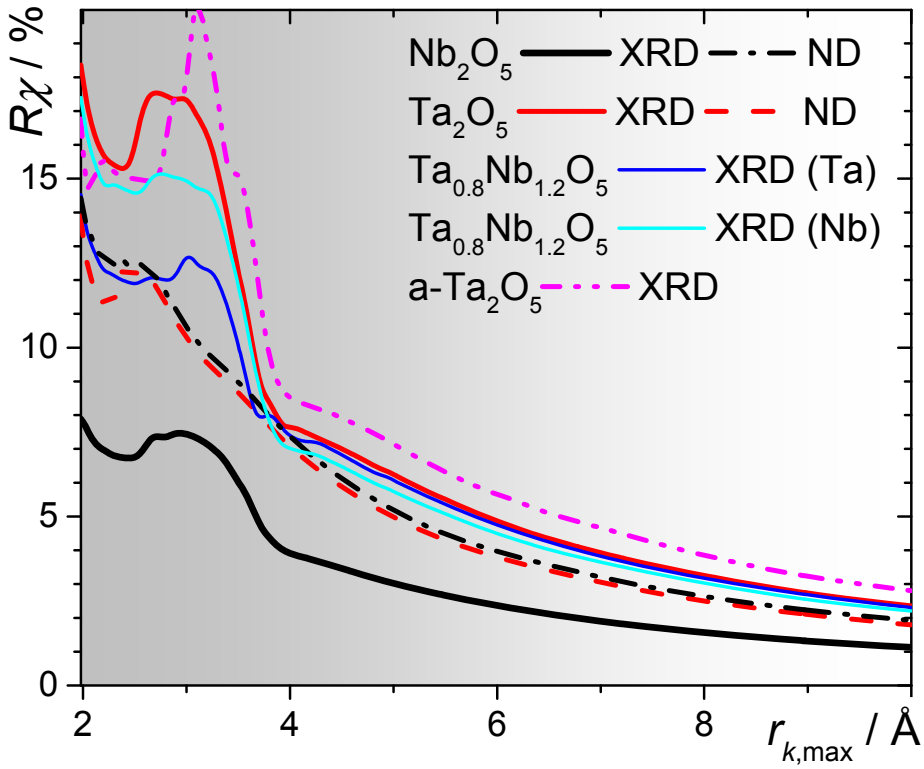

Figure 4: Goodness-of-fit parameters as a function of summation cutoff radius for various EPSR models.

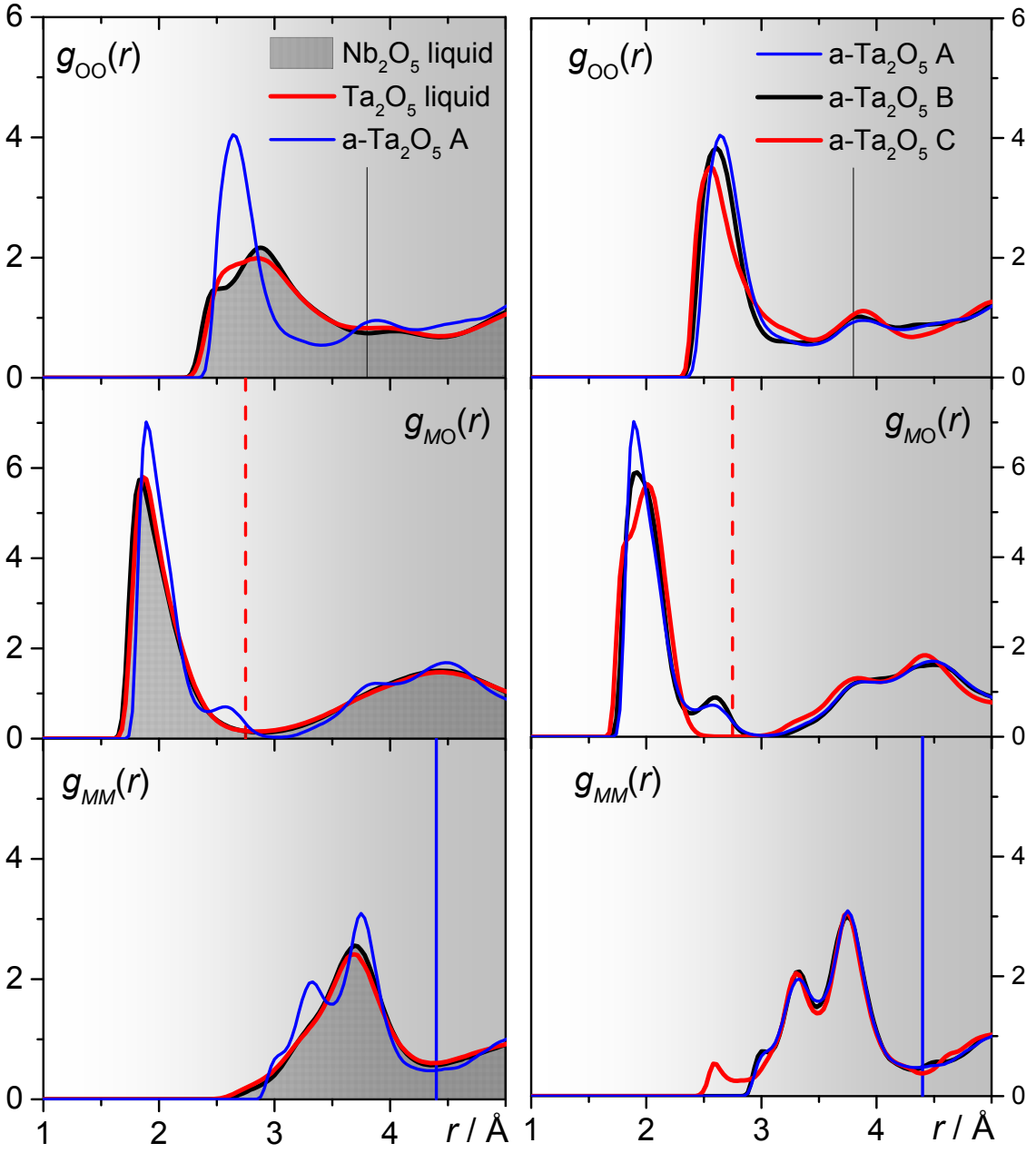

Figure 5: Partial pair distribution functions derived by EPSR for the a-Ta_2O_5 IBS film and molten Ta_2O_5 and Nb_2O_5 liquids. Vertical lines correspond to cutoff radii for which coordination number and bond-angle distributions were calculated.

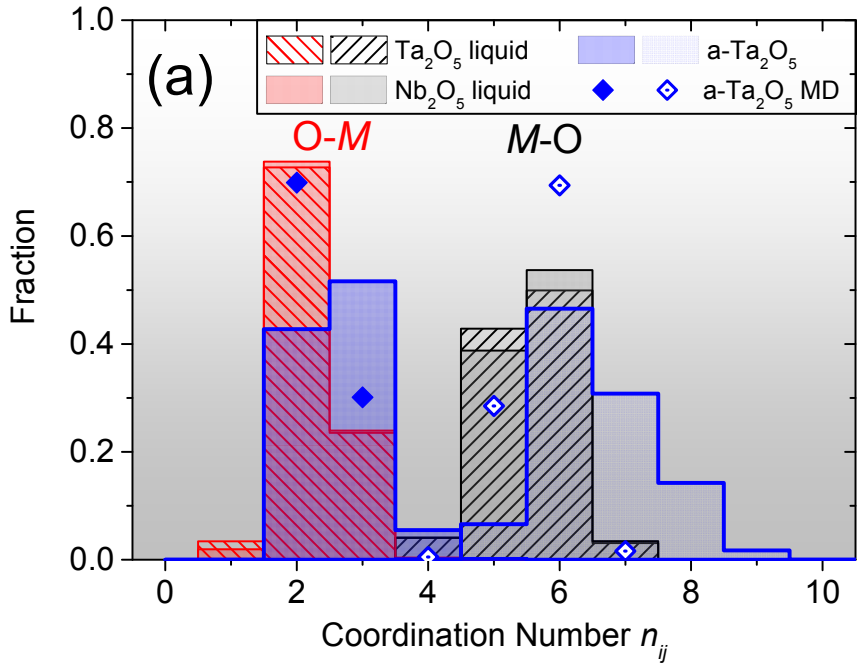
(a)
Ta2O5 liquid
Nb2O5 liquid
a-Ta2O5
a-Ta2O5 MD
O-M
M-O
Fraction
Coordination Number nij
1.0
0.8
0.6
0.4
0.2
0.0
0
2
4
6
8
10

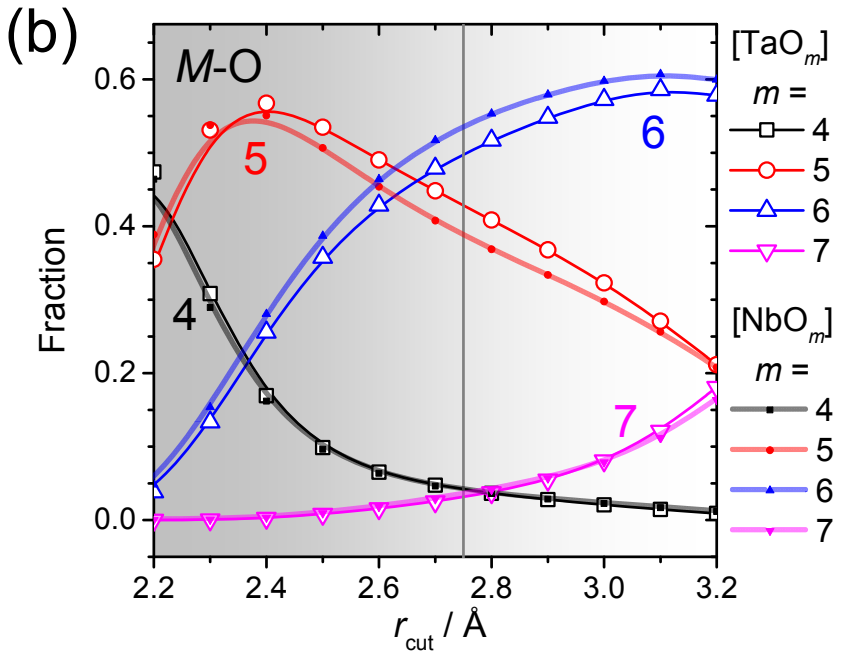
(b)
M-O
5
6
4
7
Fraction
rcut / Å
[TaOm]
m =
4
5
6
7
[NbOm]
m =
4
5
6
7
0.6
0.4
0.2
0.0
2.2
2.4
2.6
2.8
3.0
3.2

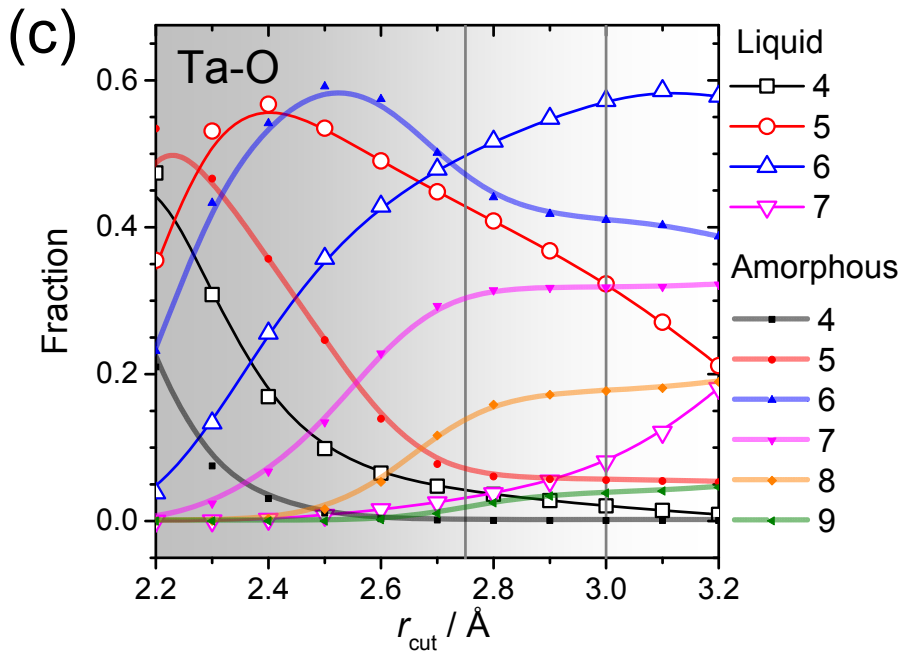

Figure 6: Coordination number distributions for a-Ta_2O_5 IBS film and molten Ta_2O_5 and Nb_2O_5 liquids a) O–*M* and *M*–O distributions for a fixed cutoff radius of 2.75Å. Results from the MD study of Damart, et al. [9] are also shown. b) As a function of cutoff radius for the two liquids. c) As a function of cutoff radius for liquid and solid-amorphous tantala.

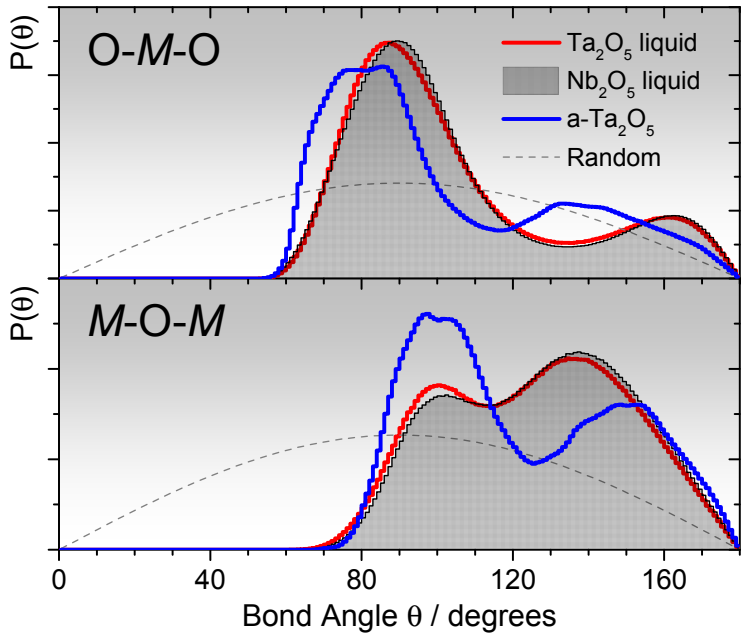

Figure 7: Bond angle distributions for a-Ta_2O_5 IBS film and molten Ta_2O_5 and Nb_2O_5 liquids.

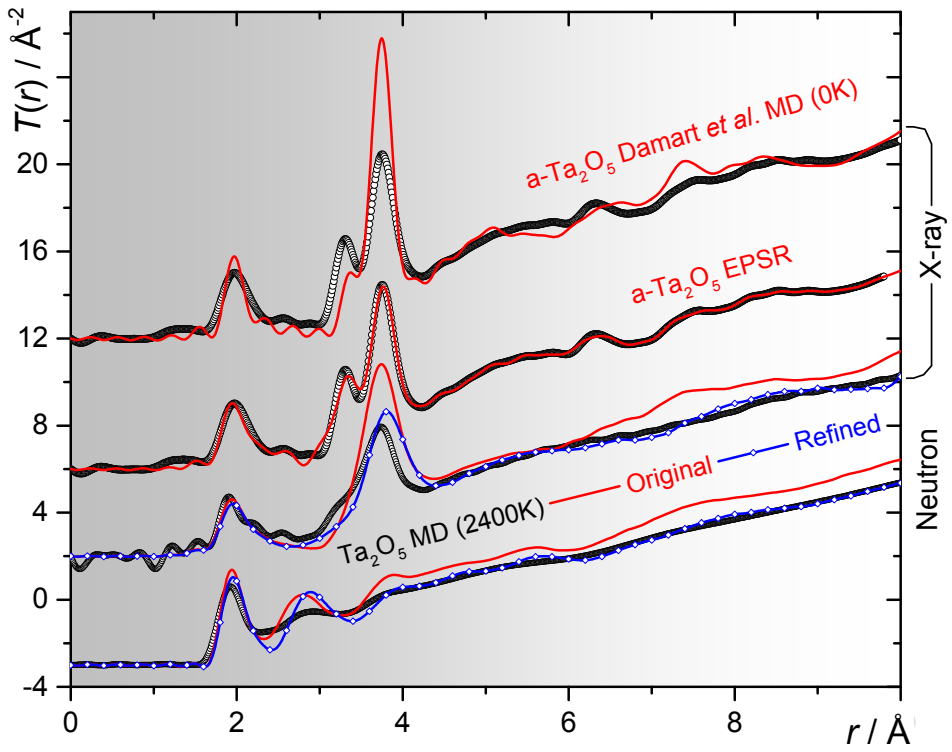

Figure 8: Total correlation functions for liquid and solid-amorphous tantala. The experimental data are repeated from Fig. 2, along with the a-Ta_2O_5 EPSR model, whilst the remaining solid curves represent MD models derived herein for the liquid and by Damart, et al. [9] for the solid, in both cases using the potentials of Trinastic, et al. [8], or refinements thereof.